

Plasmonic performance of $\text{Au}_x\text{Ag}_y\text{Cu}_{1-x-y}$ alloys from many-body perturbation theory

Okan K. Orhan¹ and David D. O'Regan¹

School of Physics, Trinity College Dublin, Dublin 2, Ireland

(Dated: 4 January 2019)

We present a detailed appraisal of the optical and plasmonic properties of ordered alloys of the form $\text{Au}_x\text{Ag}_y\text{Cu}_{1-x-y}$, as predicted by means of first-principles many-body perturbation theory augmented by a semi-empirical Drude-Lorentz model. In benchmark simulations on elemental Au, Ag, and Cu, we find that the random-phase approximation (RPA) fails to accurately describe inter-band transitions when it is built upon semi-local approximate Kohn-Sham density-functional theory (KS-DFT) band-structures. We show that non-local electronic exchange-correlation interactions sufficient to correct this, particularly for the fully-filled, relatively narrow d -bands that which contribute strongly throughout the low-energy spectral range (0 – 6 eV), may be modelled very expediently using band-stretching operators that imitate the effect of a perturbative G_0W_0 self-energy correction incorporating quasiparticle mass renormalization. We thereby establish a convenient work-flow for carrying out approximated G_0W_0 +RPA spectroscopic calculations on alloys and, in particular here, we have considered alloy concentrations down to 12.5 % in $\text{Au}_x\text{Ag}_y\text{Cu}_{1-x-y}$, including all possible crystallographic orderings of face-centred cubic (FCC) type. We develop a pragmatic procedure for calculating the Drude plasmon frequency from first principles, including self-energy effects, as well as a semi-empirical scheme for interpolating the plasmon inverse lifetimes between stoichiometries. A distinctive M-shaped profile is observed in both quantities for binary alloys, in qualitative agreement with previous experimental findings. A range of optical and plasmonic figures of merit are discussed, and plotted for ordered $\text{Au}_x\text{Ag}_y\text{Cu}_{1-x-y}$ at three representative solid-state laser wavelengths. On this basis, we predict that certain compositions may offer improved performance over elemental Au for particular application types. We predict that while the loss functions for both bulk and surface plasmons are typically diminished in strength through binary alloying, certain stoichiometric ratios may exhibit higher-quality (longer-lived) localized surface-plasmons (LSP) and surface-plasmon polaritons (SPP), at technologically-relevant wavelengths, than those in elemental Au.

Keywords: Alloy Design for Plasmonics, Theoretical Spectroscopy, Many-Body Perturbation Theory

I. INTRODUCTION

Noble metals and their alloys are compelling materials for opto-electronic applications^{1–6} due to their strong plasmonic and optical response throughout the infrared-visible-ultraviolet spectral range. The tailoring of plasmonic and optical properties of metals via alloying is currently attracting interest due to a high demand for novel and more efficient nano-materials for opto-electronic applications^{7–9}. Nano-structures of pure Au, Ag and Cu are used in diverse opto-electronic applications, due to their good chemical and mechanical stabilities, as well as their strong optical response in the low-energy spectral range. Hence, their alloys are naturally expected to be promising candidates for efficient opto-electronic applications. Spectroscopic measurements on alloys are mostly performed on their thin-film surfaces^{10–19}, which are highly dependent on the alloying technique used²⁰. As a result, it is difficult to find consensus within the literature even on basic quantities such as the plasma frequency of an elemental metal.

Systematic first-principles studies of such alloys may, therefore, offer fundamental insights into the microscopic effects of alloying on optical properties, and potentially thereby even guide the tailoring of optical and plasmonic response for designated applications. This work is an exploratory investigation into the viability of such an approach using state-of-the-art theory. Specifically, in this

article, we present a detailed investigation into the capabilities and limitations of contemporary theoretical spectroscopy for noble metals, and the development and testing of a set of computationally light techniques for studying the spectra of noble metals and their ordered alloys within the linear-response regime. Taking advantage of the resulting high-throughput-compatible approach, we provide various *figures of merit* for comparing the plasmonic performance of these alloys, from which the optimal stoichiometry for a given optical or plasmonic characteristic, at a given driving frequency, may be estimated.

II. THEORETICAL METHODOLOGY

In the study and simulation of solid-state optical and energy-loss spectra, the macroscopic dielectric function $\mathcal{E}(\omega)$ is the central function due to its well-established connection to measured observables. In the low-energy spectral range, where the phenomena contributing to optical spectra are almost entirely electronic, the macroscopic dielectric function of a metallic system is constituted by two terms, explicitly by

$$\mathcal{E}(\omega) = \mathcal{E}^{\text{inter}}(\omega) + \mathcal{E}^{\text{intra}}(\omega), \quad (1)$$

where $\mathcal{E}^{\text{inter}}(\omega)$ and $\mathcal{E}^{\text{intra}}(\omega)$ result from screening effects due to inter-band transitions and intra-band transitions

(giving rise to the Drude plasmon), respectively.

When a solid is simulated as an infinite object, electronic transitions are envisaged as occurring simultaneously throughout the material, at a given energy of electro-magnetic (EM) radiation. Observable spectra are spatial averages of these transitions, whereas electronic transitions are microscopic events. Hence, an averaging process is required to connect microscopic quantities to macroscopic observables. Specifically, an averaging via the inverse dielectric function is the appropriate route to obtain the macroscopic dielectric function in the optical (vanishing momentum transfer) limit^{21,22}, and this is given, in terms of the *microscopic* dielectric matrix ε , by

$$\mathcal{E}(\omega) = \frac{1}{\lim_{\mathbf{q} \rightarrow 0} \left[\varepsilon_{\mathbf{G},\mathbf{G}'}^{-1}(\mathbf{q}, \omega) \right]_{\mathbf{G},\mathbf{G}'=0}}. \quad (2)$$

As the momentum \mathbf{q} transferred from the incoming photon is assumed to be negligible, only vertical excitations at each point in reciprocal space are considered here. Notwithstanding, non-local screening ‘local field’ effects are explicitly incorporated by means of Eq. 2. Where such effects can be safely neglected, we may use the relatively simple, conveniently inversion-free formula

$$\mathcal{E}(\omega) \approx \lim_{\mathbf{q} \rightarrow 0} [\varepsilon_{\mathbf{G},\mathbf{G}'}(\mathbf{q}, \omega)]_{\mathbf{G},\mathbf{G}'=0}. \quad (3)$$

A. Inter-band transitions

Inter-band transitions are electronic transitions between the valence (occupied) and conduction (unoccupied) bands. Within the linear-response regime that typically holds for photon energies in the IR-vis-UV range, the inverse microscopic dielectric function is given, in reciprocal space, by the expression

$$\varepsilon_{\mathbf{G},\mathbf{G}'}^{-1}(\mathbf{q}, \omega) = \delta_{\mathbf{G},\mathbf{G}'} + v_{\mathbf{G},\mathbf{G}'}(\mathbf{q}) \chi_{\mathbf{G},\mathbf{G}'}(\mathbf{q}, \omega), \quad (4)$$

where the bare Coulomb interaction takes the form

$$v_{\mathbf{G},\mathbf{G}'}(\mathbf{q}) = \frac{4\pi}{|\mathbf{q} + \mathbf{G}| |\mathbf{q} + \mathbf{G}'|}. \quad (5)$$

In order to calculate $\varepsilon_{\mathbf{G},\mathbf{G}'}(\mathbf{q}, \omega)$, the non-interacting random-phase approximation (RPA) (Fermi’s Golden Rule)²³ linear-response function for inter-band excitations is first calculated, in terms of independent-particle wave-functions $|\psi_{v,\mathbf{k}}\rangle$ with occupancies $f_{v,\mathbf{k}}$, as^{21,22},

$$\begin{aligned} \chi_{\mathbf{G},\mathbf{G}'}^0(\mathbf{q}, \omega) &= 2 \sum_{c,v,\mathbf{k}} (f_{v,\mathbf{k}} - f_{c,\mathbf{k}-\mathbf{q}}) \\ &\times \frac{|\langle \psi_{c,\mathbf{k}-\mathbf{q}} | e^{i(\mathbf{q}+\mathbf{G}) \cdot \mathbf{r}} | \psi_{v,\mathbf{k}} \rangle|^2}{\omega - \omega_{cv,\mathbf{k}\mathbf{q}} + i\Gamma}, \end{aligned} \quad (6)$$

where v (c) indicates valence (conduction) states and $\omega_{cv,\mathbf{k}\mathbf{q}} = (E_{c,\mathbf{k}-\mathbf{q}} - E_{v,\mathbf{k}})$ is a difference between single-

particle energy eigenvalues (using atomic units). Here, Γ is a small, positive-valued Lorentzian broadening factor, \mathbf{q} is the transferred momentum vector, which lies in the first Brillouin zone, and the factor of 2 pre-supposes and accounts for spin degeneracy. Following this, the *interacting* RPA^{24–27} response function χ is given by^{24–27}

$$\chi_{\mathbf{G},\mathbf{G}'}(\mathbf{q}, \omega) = \chi_{\mathbf{G},\mathbf{G}'}^0(\mathbf{q}, \omega) (1 + v_{\mathbf{G},\mathbf{G}'}(\mathbf{q}) \chi_{\mathbf{G},\mathbf{G}'}(\mathbf{q}, \omega)), \quad (7)$$

which is a Dyson equation. Eq. (7) may be rearranged into the compact form, involving matrix inversion, of

$$\chi^{-1}(\mathbf{q}, \omega) = \chi_0^{-1}(\mathbf{q}, \omega) - \mathbf{v}(\mathbf{q}). \quad (8)$$

for the interacting response function. Alternatively, the more approximate independent-particle RPA dielectric function may be calculated as

$$\varepsilon_{\mathbf{G},\mathbf{G}'}^0(\mathbf{q}, \omega) = \delta_{\mathbf{G},\mathbf{G}'} - v_{\mathbf{G},\mathbf{G}'}(\mathbf{q}) \chi_{\mathbf{G},\mathbf{G}'}^0(\mathbf{q}, \omega). \quad (9)$$

When $\varepsilon \approx \varepsilon^0$ is invoked it is conventional to also neglect local-field effects, by means of Eq. 3.

B. Intra-band transitions

In addition to inter-band transitions, the promotion of electrons to higher energies within the *same* band, at finite temperatures, contributes very significantly to the macroscopic dielectric function of metallic solids within the low-energy regime. This is the intra-band transition effect, which gives rise to the prominent Drude plasmon divergence in the optical absorption spectrum in the static limit. This Drude plasmon can be thought of semi-classically as the collective oscillation of electrons at the Fermi level, in phase with the longitudinal part of the driving EM radiation. The Drude plasmon typically occurs at ~ 10 eV in elemental late transition metals, and it can be excited, e.g., by energy loss of incident electrons with kinetic energies in the 1–20 keV range, or by using lasers tuned to the plasmon wavelength.

The direct simulation of a well-converged Drude plasmon frequency starting a set of single-particle electronic states is computationally demanding, indeed extremely so due to the requirement for dense Brillouin-zone sampling at and around the Fermi surface, for example up to ~ 16000 grid points in Ref. 28. This procedure is not commonly followed, as the resulting intra-band dielectric function remains excessively sensitive to the difficult-to-estimate excitation damping (or lifetime) factor that must be imposed. The Drude plasmon lifetime is limited by a multitude of physical processes, in reality, including scattering by phonons, defects, and grain boundaries; electron-electron (including electron-plasmon and plasmon-plasmon) scattering giving rise to decay, and quantum thermodynamic effects.

More commonly, the Drude plasmon is discussed in terms of a classical model for free electrons oscillating under the influence of external electric field, namely the

Drude-Lorentz model^{29–32}. The Drude plasmon contribution to the macroscopic dielectric function becomes

$$\mathcal{E}^{\text{intra}}(\omega) = \varepsilon_\infty - \frac{\omega_p^2}{\omega^2 - i\eta_p\omega}, \quad (10)$$

where ω_p , η_p , and ε_∞ are the Drude plasmon energy (not to be confused with the actual net plasma frequency of the metal – where $\Re[\mathcal{E}(\omega)] \approx 0$ eV), the phenomenological inverse life-time, and the electric permittivity in the infinite-frequency limit, respectively. The set $\{\omega_p, \eta_p, \varepsilon_\infty\}$ comprise the ‘Drude parameters’. Experimentally, it is standard practice is to perform optical (e.g., n and k) measurements within the infrared and the far-infrared spectral range (corresponding to $\omega \approx 0 - 2$ eV), and to determine these parameters by fitting to the Drude-Lorentz model^{33–39}.

Inspired by this, here, we start from the Drude plasmon energy in Eq. (10), which can be expressed as^{29,30,40}

$$\omega_p^2 = \frac{4\pi N(E_F)}{m_{\text{eff}}}, \quad (11)$$

for a uniform non-interacting electron gas. In this, $N(E_F)$ is the density of states (DOS) at the Fermi level and m_{eff} is the electron effective mass. In practice, for real metals, this effective mass is also evaluated at the Fermi level and, if we further assume that the metallic bands have a parabolic dispersion normal to the Fermi surface⁴¹, we may write

$$\begin{aligned} m_{\text{eff}}^{-1} &\approx \frac{1}{3} \langle v^2(E_F) \rangle \\ &= \frac{1}{3} \left(\sum_i \int_{S_{F_i}} d\mathbf{k} v_i^2(\mathbf{k}) \right) \left(\sum_j \int_{S_{F_j}} d\mathbf{k}' \right)^{-1}, \\ \text{if } v_i^2(\mathbf{k}) &= \left| \frac{\partial E_{i,\mathbf{k}}}{\partial \mathbf{k}} \right|^2. \end{aligned} \quad (12)$$

Here, S_{F_i} signifies the Fermi surface of the i^{th} metallic band, and the factor of $1/3$ results from the squared Fermi velocity being averaged (rather than summed) over Cartesian directions. Succinctly, the Drude plasmon energy can thus be approximated within a non-interacting, uniform-gas theory, simply and efficiently as⁴¹

$$\omega_p^2 = \frac{4\pi}{3} N(E_F) \langle v^2(E_F) \rangle. \quad (13)$$

As previously mentioned, the routine direct calculation of experimentally-relevant Drude plasmon lifetimes for is currently beyond the scope of state-of-the-art electronic structure simulation methodology. Electron-phonon and electron-impurity scattering typically dominantly contribute to the limiting DC conductivity σ_0 , as compared to the more accessible electron-electron scattering processes⁴⁰. In order to circumvent this issue, we have developed a semi-empirical scheme based upon the Drude-Lorentz model, in which the scattering rate η_p is inversely

proportional to the DC conductivity and to the effective mass of carriers, but proportional to their concentration. Noting a very plausible linear dependence between σ_0 and $\sqrt{\langle v^2(E_F) \rangle}$, we express the scattering rate (where the first equality is standard Drude-Lorentz) as

$$\eta_p = \frac{N(E_F)}{\sigma_0 m_{\text{eff}}} \approx c_\eta N(E_F) \langle v^2(E_F) \rangle^{1/2}, \quad (14)$$

where c_η is our scaling coefficient to be determined.

Next, separating the real and imaginary part of $\mathcal{E}^{\text{intra}}(\omega)$ from Eq. (10), we arrive at

$$\begin{aligned} \Re[\mathcal{E}^{\text{intra}}] &= \mathcal{E}_1^{\text{intra}}(\omega, \omega_p, \eta_p, \varepsilon_\infty) = \varepsilon_\infty - \frac{\omega_p^2}{\omega^2 + \eta_p^2}, \\ \Im[\mathcal{E}^{\text{intra}}] &= \mathcal{E}_2^{\text{intra}}(\omega, \omega_p, \eta_p) = \frac{\eta_p \omega_p^2}{\omega^3 + \eta_p^2 \omega}, \end{aligned} \quad (15)$$

and note that, given the first-principles ω_p , the imaginary part is parametrized only by η_p . Thus, in practice, we first determine the scaling factor c_η for η_p in Eq. (14) by least-squares fitting against $\mathcal{E}_2^{\text{intra}}$ from an appropriate experimental spectrum within the near infra-red spectral range (we find that $\omega \approx 0.8 - 1.2$ eV is very effective for noble metals – but we emphasize that the choice of regression domain does matter). Secondly, we determine ε_∞ by fitting $\mathcal{E}_1^{\text{intra}}$ to the same experimental spectrum, using the fixed values for ω_p and η_p obtained in the previous step, within the same spectral range. In practice, we have found this two-step procedure to be quite reliable, whereas simultaneous least-squares regression of c_η and ε_∞ against the complex-valued $\mathcal{E}^{\text{intra}}(\omega)$ can yield unphysical values for both parameters.

C. Treatment of non-local many-electron effects within the quasi-particle formalism: Perturbative one-shot GW: G_0W_0

In order to calculate the aforementioned response functions, e.g. in Eq. 6, a sufficiently complete set of well-defined single-particle electronic states is required. Density functional theory (DFT)⁴² is currently the almost-ubiquitously used approach for constructing ground-state electronic structures of solids within its Kohn-Sham formalism (KS-DFT)⁴³. However, the DFT is limited by the accuracy of available, computationally feasible local and semi-local approximations for exchange and correlation^{43–46}. Furthermore, the energy eigenvalues (band-structures) generated by the Kohn-Sham mapping have no formal meaning in terms of electron addition or removal energies (except in certain well-documented instances), in spite of their being widely interpreted as such. The RPA, although it is a true many-body approximation, is unable to build any electron or hole quasi-particle^{47–49} screening (e.g. electron-plasmon coupling) effects into an underlying Kohn-Sham eigensystem, as it

treats only the screened interaction between *pairs* of such input particles. The fact that the absence of non-local quantum many-body effects in semi-local KS-DFT, and absent explicit long-ranged exchange in particular, often leads to inaccurate descriptions of the electronic bands in solids is well reported for various material classes, such as insulators and semi-conductors^{50–54}, transition-metal oxides^{55–57}, and metallic solids^{58,59}.

In noble metals, the electronic bands that dominantly contribute to low-energy spectra are fully-filled d^{10} bands tightly packed in a narrow energy window close to the Fermi level. It has previously been found that these electronic bands are poorly described within approximate KS-DFT for noble metals such as bulk Au⁶⁰, and then that such errors become more pronounced in spectral simulations using the RPA^{61–65}. The formally correct approach to calculating band-structures from first principles is instead the quasiparticle (QP) formalism, fundamental to which is a mapping of the interacting many-body system to a weakly-interacting many-body system of virtual ones, namely the quasi-particles^{66,67}. QP wave-functions and corresponding energy levels can be determined by self-consistently solving the QP equation

$$\left[-\frac{1}{2m_{\text{QP}}} \nabla_i^2 + v_{\text{ext}}(\mathbf{r}) + v_H(\mathbf{r}) + \int d\mathbf{r}' \Sigma(\mathbf{r}, \mathbf{r}', \omega) \right] \psi_i^{\text{QP}}(\mathbf{r}, \omega) = \epsilon_i^{\text{QP}} \psi_i^{\text{QP}}(\mathbf{r}, \omega), \quad (16)$$

where $\Sigma(\mathbf{r}, \mathbf{r}', \omega)$ is the energy-dependent, non-local, and non-Hermitian self-energy. The resulting $\Psi_i^{\text{QP}}(\mathbf{r})$ and E_i^{QP} are the i^{th} QP wave-function and the corresponding QP energy. In practice, QP energies are more commonly calculated using nonetheless demanding many-body perturbation theory (MBPT)⁶⁸ methods with Green's functions instead of explicit solution of Eq. (16).

The GW approximation is the cornerstone of MBPT for electrons. In GW, the self-energy is calculated in one iteration formally as

$$\Sigma = iGW, \quad (17)$$

where the product here is in real space and time. The screened Coulomb interaction W consistent with the GW approximation is that calculated within the RPA for a given Green's function G . Self-consistent GW is a computationally expensive approach that requires the solution of a Dyson equation multiple times, and that involves the inversion of large, complex, and near-singular matrices. Furthermore, it has been shown that it fails for systems with over half-filled $3d$ bands⁶⁹. A more successful, further approximation is one-shot, non-self-consistent GW, or simply G_0W_0 , which depends explicitly upon and input Green's electronic function G_0 , and stops at the first iteration of the self-energy, $\Sigma = iG_0W_0$.

In practice, this requires the choice of a suitable basis and, when all that is of interest are the QP energies, it is expedient to use the KS-DFT eigenbasis, on

the grounds that the approximate KS-DFT density is usually reasonable, even if the KS-DFT eigenspectrum, represented in the form of G_0 , is unphysical. Assuming that $\langle \psi_i | \psi_i^{\text{QP}} \rangle \approx 1$, the QP energies can furthermore be approximated as a first-order correction to the KS eigenvalues, as

$$\epsilon_i^{\text{QP}} = \epsilon_i + Z_i \langle \psi_i | \hat{\Sigma}(\epsilon_i) - \hat{v}_{\text{xc}} | \psi_i \rangle, \quad \text{where} \quad Z_i = \left[1 - \left. \frac{\partial \Sigma'(\omega)}{\partial \omega} \right|_{\omega=\epsilon_i} \right]^{-1}, \quad (18)$$

and Z_i is called the QP re-normalization factor. This factor can be thought of as the absolute value of the charge of the QP (e.g., of the electron and its screening cloud). Here, \hat{v}_{xc} is the approximate exchange-correlation potential operator of KS-DFT. The method described by this final step is called perturbative G_0W_0 , and it remains explicitly dependent on the choice of approximate functional in KS-DFT.

In practice, in the KS wave-function basis, the non-interacting single-particle Green function takes the form in the frequency domain, for $t' > t$ ²⁸,

$$G_0(\mathbf{r}, \mathbf{r}', \omega) = 2i \sum_{i, \mathbf{k}} \psi_{i, \mathbf{k}}(\mathbf{r}) \psi_{i, \mathbf{k}}(\mathbf{r}') \times \left(\frac{f_{i, \mathbf{k}}}{\omega - \epsilon_{i, \mathbf{k}} + i\delta} + \frac{1 - f_{i, \mathbf{k}}}{\omega - \epsilon_{i, \mathbf{k}} - i\delta} \right) \quad (19)$$

and, once G_0 is obtained, W_0 is calculated by using Dyson's equation starting from the bare Coulomb interaction with

$$W_0 = \varepsilon^{-1} v, \quad (20)$$

where W^0 is a function of ω through the inverse dielectric function ε^{-1} . In reciprocal space, W_0 is expressed by Eq. (5) and Eq. (9) as the direct product

$$W_{0\mathbf{G}, \mathbf{G}}(\mathbf{q}, \omega) = \varepsilon_{\mathbf{G}, \mathbf{G}'}^{-1}(\mathbf{q}, \omega) \frac{4\pi}{|\mathbf{q} + \mathbf{G}| |\mathbf{q} + \mathbf{G}'|}. \quad (21)$$

Computationally, the inversion of the dielectric function, which is a large matrix with frequency-dependent complex entities, is troublesome. Hence, the frequency-dependent complex entities are approximated by Lorentzian peaks within the plasmon-pole approximation (PPA)^{70,71}. The idea behind the PPA is to replace the single-particle transitions making up $\varepsilon_{\mathbf{G}, \mathbf{G}'}^{-1}(\mathbf{q}, \omega)$, which increase in number with the square of the system size, with a smaller number of effective plasmon modes. Thus ε^{-1} is approximated in practice via

$$\varepsilon_{\mathbf{G}, \mathbf{G}'}^{-1}(\mathbf{q}, \omega) = \delta_{\mathbf{G}, \mathbf{G}'} + \sum_{\lambda} \frac{\Omega_{\mathbf{G}, \mathbf{G}'}^{\lambda}}{\omega^2 - (\bar{\omega}_{\mathbf{G}, \mathbf{G}'}^{\lambda})^2}, \quad (22)$$

where $\Omega_{\mathbf{G}, \mathbf{G}'}$ and $\bar{\omega}_{\mathbf{G}, \mathbf{G}'}$ are the strength and the fre-

quency of plasmons fitted to the RPA inverse dielectric function. A second advantage of the PPA is that analytical formulae for Σ are available in the frequency domain.

III. COMPUTATIONAL DETAILS

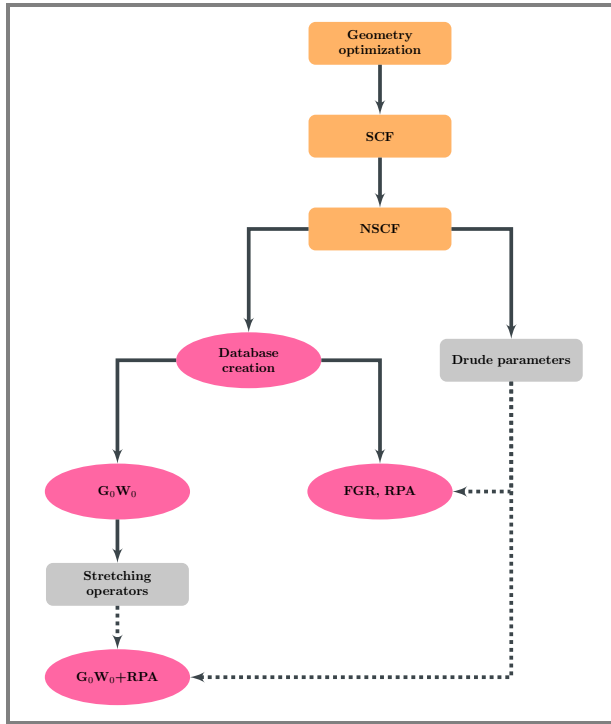


FIG. 1. The work-flow followed here to calculate the optical spectra of $\text{Au}_x\text{Ag}_y\text{Cu}_{1-x-y}$ using Quantum ESPRESSO (QE) and Yambo. Color codes are assigned to each software with QE as orange, Yambo as pink, and in-house code as gray.

Geometry optimization, self-consistent field (SCF) and non-self-consistent field (NSCF) simulations were performed using the Quantum ESPRESSO software (QE)^{72,73}. For this, norm-conserving PBE pseudo-potentials were produced using the pseudo-potential generator OPIUM⁷⁴. The initial crystallographic information for bulk Au, Ag, and Cu in their FCC structures were adopted from X-ray diffraction data at 1072 K from Ref. 75, for consistency with choice of smearing parameter for the Marzari-Vanderbilt cold smearing⁷⁶, namely 0.1 eV. Full geometry relaxations were then performed with variable cell parameters at over-converged plane-wave cutoff energies ($E_{\text{cut}} = 75$ Ha) with automatically generated $4 \times 4 \times 4$ uniform Monkhorst-Pack Brillouin zone sampling, without imposing any crystal symmetry.

For band-structure calculations, we moved down to a plane-wave cutoff energy of $E_{\text{cut}} = 25$ Ha, which is sufficient to attain a total-energy tolerance of $\Delta E_{\text{tot}} \leq 0.001$ Ha per atom, but up to a uniform Brillouin zone sampling of $16 \times 16 \times 16$ at the NSCF level, which was nec-

essary to converge the expectation value of the exchange self-energy. Experimental spectra have large inter-band smearing Γ values due to finite temperature effects and impurities in practice^{32,77,78}. Hence, a Lorentzian smearing parameter of full-width 0.2 eV was adopted for spectral simulation with the Yambo code⁷⁹. Final simulations with a common set of parameters were performed on Au, Ag, and Cu for benchmarking the various levels of theory studied, against experimental spectra. The work-flow for simulations of spectra with FGR, RPA and G_0W_0 +RPA is illustrated in Fig. 1.

IV. WORK-FLOW OPTIMIZATION AND BENCHMARKING ON PURE METALS: AU, AG, AND CU

For noble metals, we have found that even a converged inaccurate semi-local KS-DFT description of the relevant quasiparticle bands requires demanding run-time parameters and accurate pseudopotentials. Therefore, when larger crystallographic unit cells are of interest such as for the alloys central to this work, even perturbative G_0W_0 becomes computationally impractical, and we cannot routinely go very far beyond KS-DFT in terms of computational overhead. Hence, here, we have pursued an intermediate, compromise approach in which non-local quasiparticle screening effects are incorporated approximately, in a scaleable manner which incurs a minimum additional computational cost that is insignificant compared to the final RPA calculation for the spectrum.

In principle, G_0W_0 +RPA spectra require a full QP band-structure as a starting point. To obtain the QP band-structure, we would need to evaluate QP energies for each point in the Brillouin zone, for every band. For a given band and point in the Brillouin zone $\{i, \mathbf{k}\}$, such an operation consists of summing throughout the Brillouin zone and over bands to determine G_0 , as well as W_0 through the inverse dynamic dielectric function for the self-energy operator in Eq. (18). Such a task is highly demanding both in terms of CPU hours as well as RAM. This operation needs to load all information about KS wave-functions in each processor unit, when using Yambo. Since our eventual goal here is to construct optical spectra rather than QP bands, an averaged stretching to underlying KS band-structure via stretching operators close to the Fermi level is sufficient, as well as more feasible for the spectral range of interest. The idea of stretching operators is to approximate QP energies as linear-functions of the KS energies, and for metals in particular we have simply

$$\epsilon_v^{\text{QP}} = s_v \epsilon_v, \quad \text{and} \quad \epsilon_c^{\text{QP}} = s_c \epsilon_c, \quad (23)$$

where s_v and s_c are separate stretching factors for the valence and conduction bands, respectively. Such an approach introduces averaged corrections to the valence and conduction bands around Fermi level for the missing non-

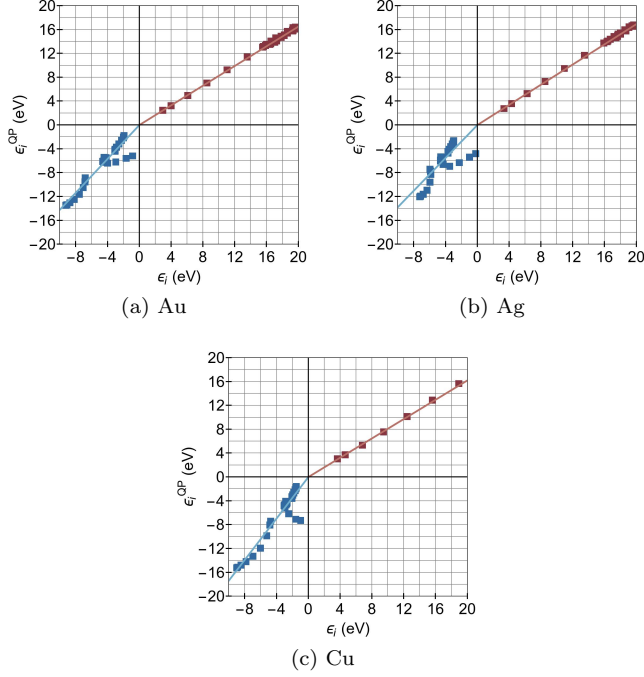


FIG. 2. Determination of the stretching operators for Au, Ag, and Cu by means linear fitting to KS-DFT vs. QP eigen-energies using 10 points around the Γ point for 6 valence (blue points) and 6 conduction (red points) bands. The Fermi levels are shifted to 0 eV in each case.

local electronic exchange-correlation effects, whilst keeping the Fermi level fixed. The stretching operators were determined by linear regression on ϵ_i vs. ϵ_i^{QP} . For pure metals, QP energies were calculated for 6 valence bands and 6 conduction bands at 10 points at and around Γ , and the stretching operators were determined by linear fitting as shown in Fig. 2 with the values listed in Table I. In Fig. 2, two branches are observed in the valence manifolds. These distinctive branches are due to different non-local exchange contributions to s and d -bands, but nonetheless a single stretching factor proved to be adequate.

	s_v	s_c
Au	1.419797	0.825253
Ag	1.376302	0.846172
Cu	1.735804	0.809883

TABLE I. Calculated values for stretching operators used to stretch KS band-structures in order to imitate perturbative G_0W_0 QP band-structures for pure Au, Ag, and Cu.

The stretching operators modify the KS band-structure as shown in Fig. 3. The Fermi-Dirac distribution for the chosen electronic temperature was used to in-

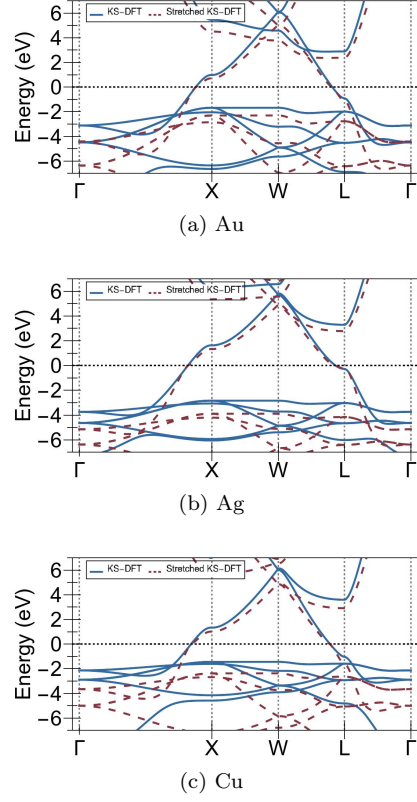


FIG. 3. KS and QP band-structures for Au, Ag, and Cu along a high-symmetry path with a 0.001 a_0^{-1} step size.

terpolate between the distinct stretching parameters for the valence and conduction bands. KS-DFT tends to excessively flatten the fully filled d -bands due to an absence of attractive non-local exchange. In a sense, the stretching operator approximately corrects the dispersions of the bands, particularly for the occupied d -bands but also for the half-occupied s -band, which is made less dispersive. In Fig. 3c for Cu, the bands close to the Fermi level are more narrowly packed and flattened compared to those of Ag and Au cases, reflecting the fact that the error in the KS-DFT treatment, and hence s_v^{Cu} , is the largest amongst the three. The inverse behaviour is seen, however, for the conduction stretching operators of pure metals, which is due to correlation effects only, as Ag has the largest stretching factor in the conduction manifold, albeit that the differences between the metals are less pronounced here.

A. Drude parameters for pure metals

Before constructing optical spectra, the Drude parameters are needed for the intra-band part of the dielectric function in Eq. (15). Our first step is to calculate the Drude plasmon energies using Eq. (13). For this purpose, the energies of bands crossing the Fermi level at each k-point were extracted from the output of NSCF cal-

culations and interpolated on a fine grid in the Brillouin zone (601 points in each reciprocal-space direction), and the Fermi surface was located on this grid with a ± 0.01 eV tolerance for each system. Then, the square of the Fermi velocities, averaged over the Fermi surface, were calculated by means of Eq. (12). The calculated Fermi velocities for pure Au, Ag, and Cu are listed in Table II along with results of Ref. 80, which uses a similar procedure with an extremely dense Brillouin zone sampling as $200 \times 200 \times 200$ rather than interpolating, as we have. Furthermore, the average Fermi velocity magnitudes for QP band-structures were approximated by applying the geometric averages (more appropriate to simulate intra-band response than the arithmetic mean) of the valence and conduction stretching operators, specifically using the formula

$$v^{G_0W_0}(E_F) = \sqrt{s_v s_c} v^{KS}(E_F). \quad (24)$$

	$v^{KS}(E_F)$	$v^{G_0W_0}(E_F)$	$v^{Gall}(E_F)^{80}$
Au	13.476	14.588	13.82
Ag	13.912	15.014	14.48
Cu	10.794	12.798	11.09

TABLE II. The average Fermi velocities (in $\times 10^5$ m/s units) for pure Au, Ag, and Cu. We have included results from the work of Gall⁸⁰ (the third column), who evaluated the Fermi velocities using a $200 \times 200 \times 200$ Brillouin zone sampling.

Our averaged KS-DFT Fermi velocities slightly underestimate those of Ref. 80, as shown in the third column of Table II, and the origin of this discrepancy is not evident. Considering the much smaller computational cost of our interpolation scheme, our values are very reasonable estimates of the Drude plasmon energies. Lastly, the DOS based on the KS band-structures and QP band-structure were extracted by applying a 0.1 eV Lorentzian broadening using a post-processing tool of Yambo. Using Eq. (13), the Drude plasmon energies were estimated for the KS band-structures and QP band-structures with their respective DOS at the Fermi level.

The next step is to approximate the inverse life-time of the Drude plasmon, as well as the electric permittivity in the infinite-frequency limit, using our semi-empirical approach illustrated in Fig. 4. Scaling factors for the inverse life-times η_p in Eq. 14 were determined by fitting the imaginary part of the dielectric function to the experimental curves in Ref. 81, and then ε_∞ values were determined by fitting the real part of the dielectric function with sets of $\{\omega_p, \eta_p\}$ to the same experimental curves for Au, Ag, and Cu. The resulting values for FGR, RPA and G_0W_0 +RPA are summarized in the Supporting Information (SI).

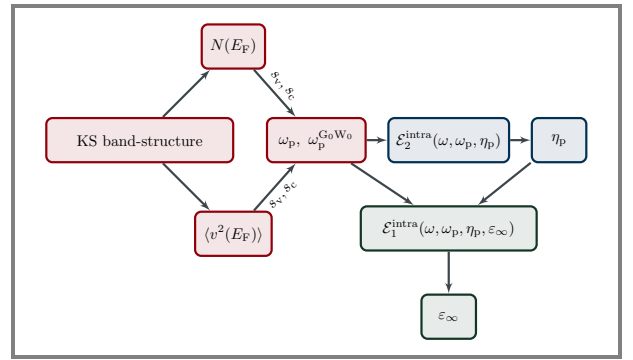


FIG. 4. A schematic of the semi-empirical method used to obtain Drude parameters for pure metals.

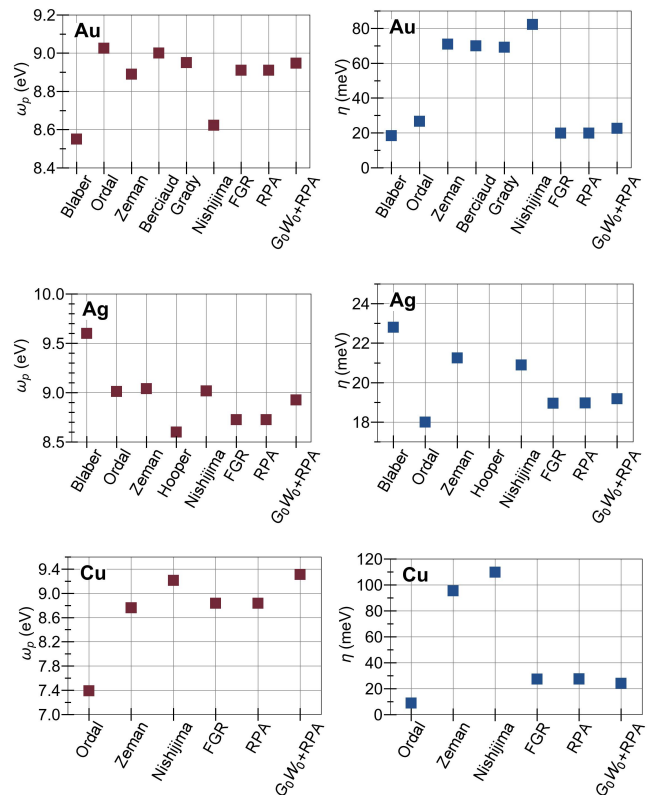


FIG. 5. Comparison of the Drude plasmon energies and inverse life-times against commonly-used experimental values for these parameters, specifically from Blaber³⁹, Ordal³³, Zeman³⁴, Berciaud³⁶, Grady³⁷, Hooper³⁵, and Nishijima¹⁹.

In experimental studies, the Drude parameters are commonly determined by least-squares fitting of the Drude-Lorentz model in Eq. (15) to measurements in the IR spectral range. Such measurements are highly sensitive to experimental details, and the resulting literature for the Drude parameters is not in good consensus as shown Fig. 5. This figure shows that, despite the relative simplicity of the approaches adopted in this work, our Drude parameters are comparable with experimental

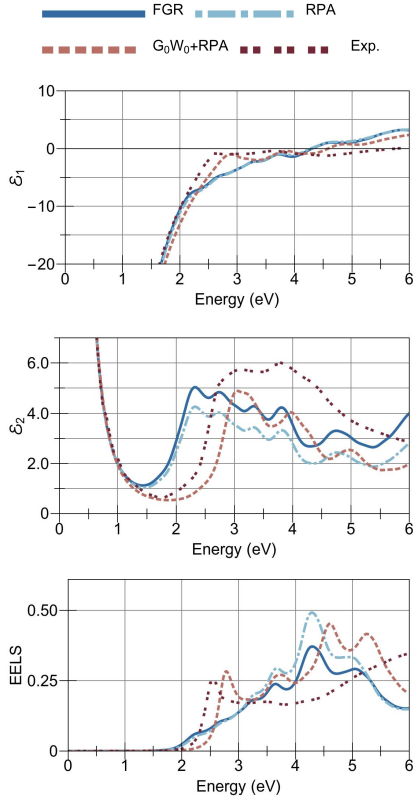


FIG. 6. The real and imaginary parts of the dielectric function and EELS for bulk Au, calculated using FGR, RPA, and G_0W_0 +RPA together with experimental data from Babar⁸¹.

predictions (particularly those of Ordal³³).

B. Optical spectra of pure metals

The spectra of our elemental metals were obtained by applying FGR and RPA to the approximate KS-DFT band-structures, and RPA upon our approximate QP band-structures. The real and imaginary part of the total dielectric function are shown for pure metals in Figs. 6, 7, and 8, along with the experimental spectra from the detailed work by Babar and Weaver in Ref. 81. Also, the electron energy-loss spectrum (EELS)^{24–26,82–85} is shown, as calculated using the relation⁵²

$$\text{EELS}(\omega) = -\text{Im} [\mathcal{E}^{-1}(\omega)]. \quad (25)$$

For all three systems, both FGR and RPA predict the lowest band-to-band absorptions to be at energies ~ 0.5 - 1.5 eV lower than those of the experimental absorption spectra. Furthermore, for higher energies, both approaches produce strong absorption peaks that contradict experiments. On the other hand, G_0W_0 +RPA locates the low-lying peaks at ~ 3 - 4 eV in Au, at ~ 4 - 5 eV in Ag, and at ~ 2 - 3 eV in Cu more accurately, and does well for the overall curve trend, with respect to the experimental absorption spectra. All three approaches

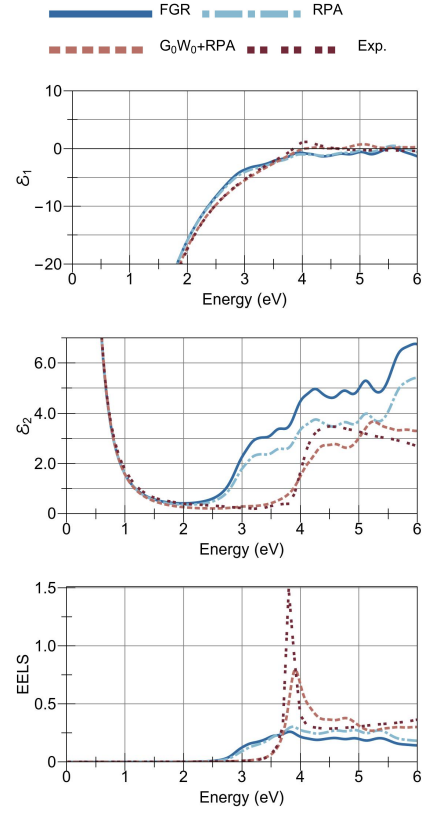


FIG. 7. The real and imaginary parts of the dielectric function and EELS for bulk Ag, calculated using FGR, RPA, and G_0W_0 +RPA together with experimental data from Babar⁸¹.

reproduce the behaviour of $\mathcal{E}_1^{\text{Cu}}$ and $\mathcal{E}_1^{\text{Au}}$ successfully, and particularly so for $\mathcal{E}_1^{\text{Ag}}$. Such improvements, along with the very substantial improvement in \mathcal{E}_2 given by G_0W_0 +RPA, lead us to locate the first plasmonic peaks in all systems quite accurately in EELS, where FGR and RPA miss the salient features completely (see Figs. 6, 7, and 8). As one can observe, the improvements provided by G_0W_0 +RPA become less effective at higher energies, although some improvements are still achieved with respect to FGR and RPA. This depletion of performance at higher energies is to be expected, as the QP band-structures were approximated using an averaged stretching factor determined using only bands close to the Fermi level. Hence, by construction, our streamlines approach is more effective for transitions between bands close to the Fermi level, which constitute the lower part of the spectra, which are always those relevant to practical plasmonic applications.

V. SPECTRA OF $\text{Au}_x\text{Ag}_y\text{Cu}_{1-x-y}$ ALLOYS

Initial geometries for selected ordered alloys with compositions in multiples of 12.5% were constructed by using super cells of pure metals and substituting the desired

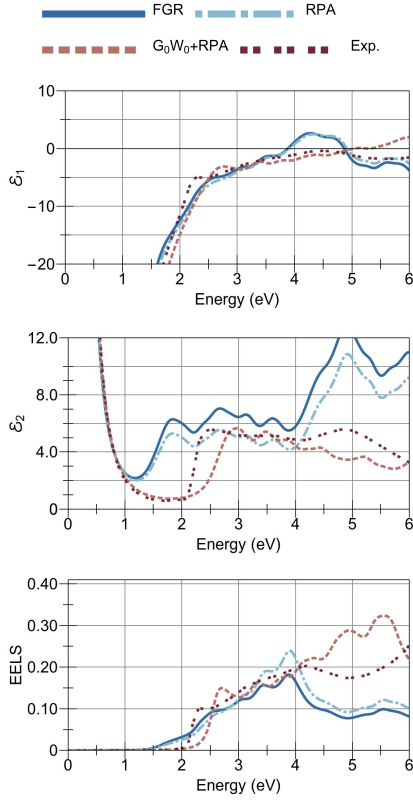


FIG. 8. The real and imaginary parts of the dielectric function and EELS for bulk Cu, calculated using FGR, RPA, and G_0W_0 +RPA together with experimental data from Babar⁸¹.

number of atoms of other species to achieve primitive unit cells for each stoichiometric ratio. These geometries were optimised at the DFT level. Sample crystal structures for each stoichiometric ratio are shown in the SI. Alloys with the stoichiometric ratios of $\{2 : 1 : 1\}$ and $\{6 : 1 : 1\}$ have 3 and 4 possible phases, respectively, and in total 39 structures were studied through the standardized work-flow shown in Fig. 1. For systems with multiple primitive phases, we calculated our final spectra by means of a thermodynamic averaging process using the Boltzmann factor defined as

$$p_i = \exp\left(\frac{E_0 - E_i}{k_B T}\right) \left(\sum_j \exp\left(\frac{E_0 - E_j}{k_B T}\right) \right)^{-1}, \quad (26)$$

where j is the phase index, and E_0 and E_i , respectively, are the lowest ground-state energy among all phases and the ground-state energy of the i^{th} phase. The final spectra of $\{2 : 1 : 1\}$ and $\{6 : 1 : 1\}$ are thus linear combinations of the spectra of their respective phases, with corresponding weighting constants.

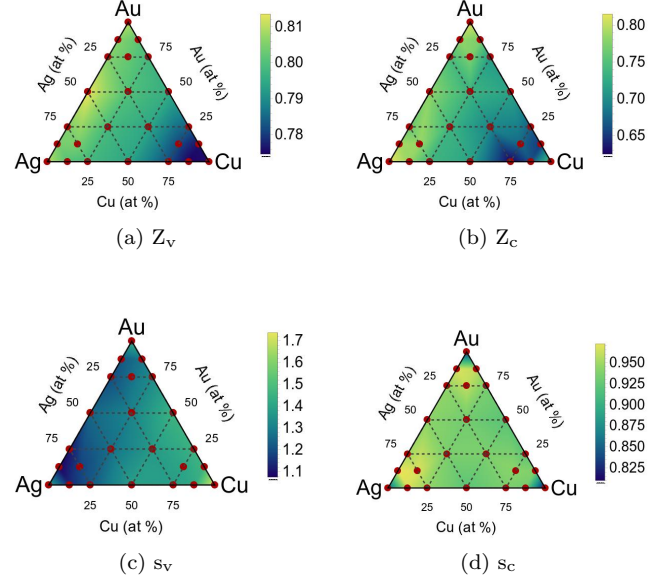


FIG. 9. Stoichiometric dependence of the averaged QP renormalization factors Z (a, and b), and corresponding stretching operators (c, and d) for chosen valence and conduction bands. The actual data points are marked with the red dots.

A. Stretching operators for alloys

Band stretching operators were calculated for all valence bands and an equal number of conduction bands at 10 points at and around the Γ point for each crystal structure of each stoichiometric ratio. The QP renormalization factors expressed in Eq. (18) show a steady decreasing trend with increasing Cu ratio, both in the valence and the conduction manifolds, as shown in Fig. 9a and Fig. 9b. The valence stretching operator in Fig. 9c grows significantly larger for increasing Cu ratios. Pure Cu has the largest reciprocal unit cell, where the d -bands are spuriously flattened and narrowly packed the most by KS-DFT, as seen in Fig. 3c. Hence, a larger QP stretching of the valence manifold is expected to result from an increasing Cu concentration. The conduction stretching operators show inverse trends, providing a slightly smaller stretching at the conduction manifold for increasing Cu concentrations. The stretching operators were applied to converged geometry of each ordered alloy cell, and perturbative G_0W_0 simulations were performed to construct the stretched (QP) band-structures individually. For simplicity, we will only discuss our approximated QP results from here, omitting FGR and RPA.

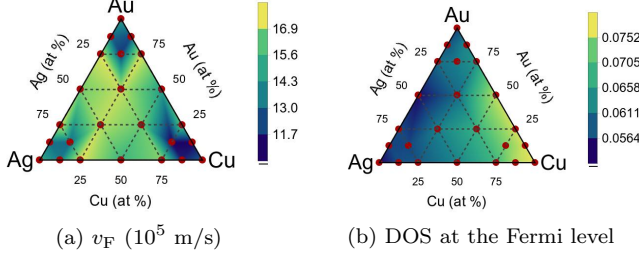


FIG. 10. Stoichiometric dependence of the averaged QP Fermi velocities and DOS at the Fermi level (dimensionless). The actual data points are marked with the red dots.

B. Drude parameters for alloys

Using a similar procedure to that of pure metals, the Fermi velocities and DOS at the Fermi level were computed for each alloy system. The stoichiometric dependence of the averaged QP Fermi velocities and DOS at the Fermi level are shown in Fig. 10. The Fermi velocities show some symmetric features, while they are lower in the case of predominantly Cu-based stoichiometric ratios. Conversely, the DOS becomes large for increasing Cu ratios as the volumes of the systems are also contracting with increasing Cu concentrations.

Competing trends in the Fermi velocities in Fig. 10a and DOS in Fig. 10b compensate each other, and lead to a symmetric trend in the interpolated contour-plot of the Drude plasmon energies in Fig. 11a. The inverse life-times in Fig. 11b were evaluated by using Eq. (14), where $\{c_\eta\}$ coefficients were produced via arithmetical averaging of the inverse-life times of pure metals with respect to the stoichiometric ratios as

$$c_\eta^{(\text{Au}_x\text{Ag}_y\text{Cu}_{1-x-y})} = (xc_\eta^{\text{Au}} + yc_\eta^{\text{Ag}} + (1-x-y)c_\eta^{\text{Cu}}) \quad (27)$$

As the inverse life-times are proportional to the Fermi velocities and the DOS at the Fermi level, they show similar symmetries to the Drude plasmon energies. The electric permittivities at the infinite-frequency limit are simply approximated by the arithmetical averaging of values of pure metals with respect to the stoichiometric ratios; hence, the trend is a flat plane by construction.

VI. PLASMONIC PERFORMANCES OF $\text{Au}_x\text{Ag}_y\text{Cu}_{1-x-y}$ ALLOYS

Even though, plasmon production is highly dependent on size and geometry of nano-materials, some fundamental criteria can be suggested as universal conditions for strong plasmonic response. The primary requirement of a strong plasmon is the presence of a high-density of free electrons such as in noble and alkali metals, which are

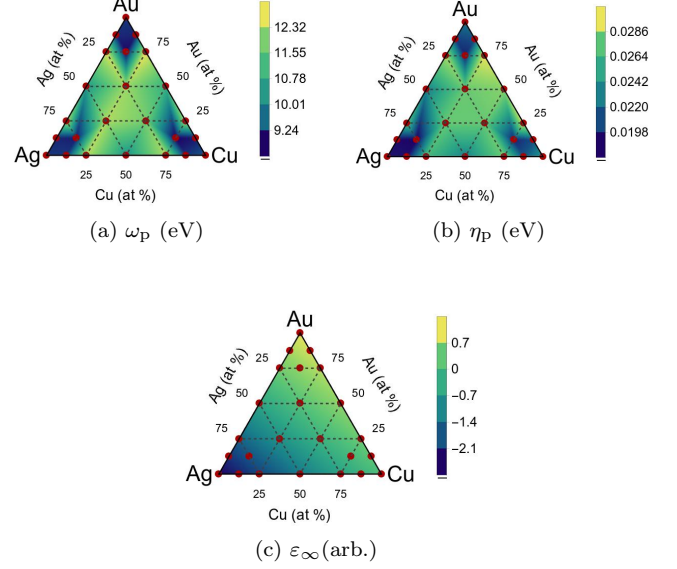


FIG. 11. Stoichiometric dependence of the averaged Drude plasmon energies, the inverse life-times and electric permittivity in the infinite-frequency limit for the QP band-structures. The actual data points are marked with the red dots.

prominent systems for plasmonic applications⁸⁶. Moreover, plasmon quality is predominantly determined by loss^{87,88}, which can occur through various phenomena such as radiative dumping, surface scattering, thermal loss⁸⁹, and imperfections in materials such as surface roughness⁹⁰, and grain boundaries⁹¹. Some approximate methods are suggested to sum individual contributions of these conditions to determine overall plasmon quality⁸⁹. As we work on perfectly ordered bulk systems, our aim is to determine some universal preliminary optical merits, which are independent of size and structural properties, to measure plasmon qualities starting from bulk dielectric functions. Plasmons in bulk systems are predominantly bulk plasmons, which is a result of a combination of both intra-band and inter-band transitions⁸⁶. The bulk plasmon energy Ω_p is expected to be at a lower energy than the bare plasmon energy ω_p due to screening of inter-band transitions. In addition to bulk plasmons, there are surface plasmons due to the finite size of realistic systems. EELS provides a signature for bulk plasmons, whereas it requires a slight modification due to the presence of *d*-bands to capture surface plasmons⁹²

$$-\Im \left[\frac{1}{1 + \epsilon} \right], \quad (28)$$

which create a condition as $\epsilon_1 \approx -1$ and $\epsilon_2 \approx 0$ for significant surface plasmons. Furthermore, some optical measures for more specific plasmons such as the localized surface-plasmon (LSP)^{93,94}, and the surface-plasmon polaritons (SPP)⁹⁵, which are crucial to many plasmonic applications⁹⁶ such as optical circuits⁹⁷ and

switching^{98,99}. In Ref. 88, various measures using the relation between \mathcal{E}_1 and \mathcal{E}_2 for LSP and SPP at low-loss and nearly an electrostatic limit have been investigated for their respective optimized geometries. \mathcal{E}_1 provides the necessary condition by checking the preliminary condition of a presence of free electrons, while \mathcal{E}_2 is related to loss due to the decaying of plasmons to particle-hole pairs via absorption. Hence, the number of electrons going through inter-band transitions is desired to be small around plasmon frequencies. Blaber, and *et al.*⁸⁶ suggest some universal quality factors for LSP and SSP in metallic systems with optimized geometries as

$$Q_{\text{LSP}}(\omega) = -\frac{\mathcal{E}_1}{\mathcal{E}_2}, \quad \text{and} \quad Q_{\text{SPP}}(\omega) = \frac{\mathcal{E}_1^2}{\mathcal{E}_2}. \quad (29)$$

These quality factors provide some preliminary insights on the capacity of metals to produce surface plasmons and life-times of such plasmons determined by dumping due to inter-band transitions.

A. Plasmonic response at common solid-state laser wavelengths

Three common solid-state laser wavelengths were chosen to demonstrate the plasmonic efficiencies of $\text{Au}_x\text{Ag}_y\text{Cu}_{1-x-y}$. The first wavelength is a common red laser at 650 nm (1.9074 eV) produced using InGaAlP¹⁰⁰ and used in a wide range of applications such as in imaging and sensing in biological systems in conjunction with a heterostructure of noble metals^{3,101}.

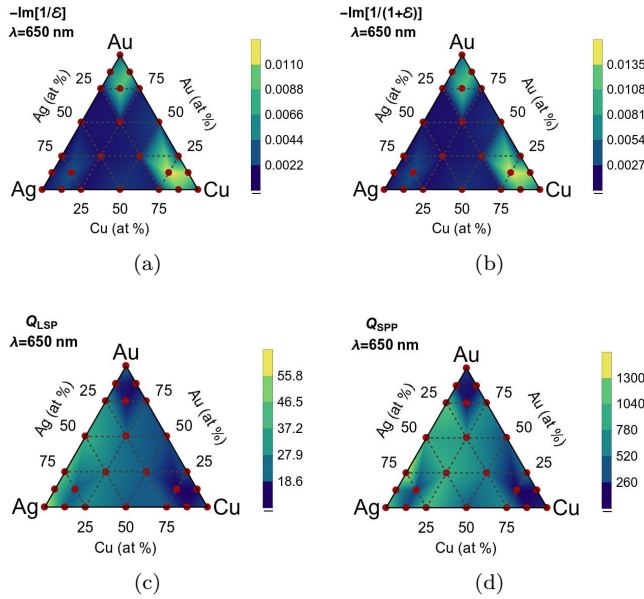


FIG. 12. Stoichiometric dependence of the averaged plasmon descriptors of bulk and surface EELS, Q_{LSP} , and Q_{SPP} for $\text{Au}_x\text{Ag}_y\text{Cu}_{1-x-y}$ at the common red solid-state laser wavelength 650 nm.

In Fig. 12, $\text{Au}_x\text{Ag}_y\text{Cu}_{1-x-y}$ alloys have weak bulk and surface plasmon resonances in orders of 10^{-2} - 10^{-3} . As this wavelength is commonly somewhere between Drude tails and inter-band transition edges of \mathcal{E}_2 , these weak plasmons have long life-times due to small radiative dumping, which result in large LSP and SPP factors. Au_6AgCu and AuAgCu_6 exhibit relatively strong plasmon resonance, whereas LSP and SPP have poor quality factors at these stoichiometric ratios due to larger losses at this wavelength. Pure Ag exhibits large quality factors for LSP and SPP; however, plasmonic resonances are quite weak at 650 nm.

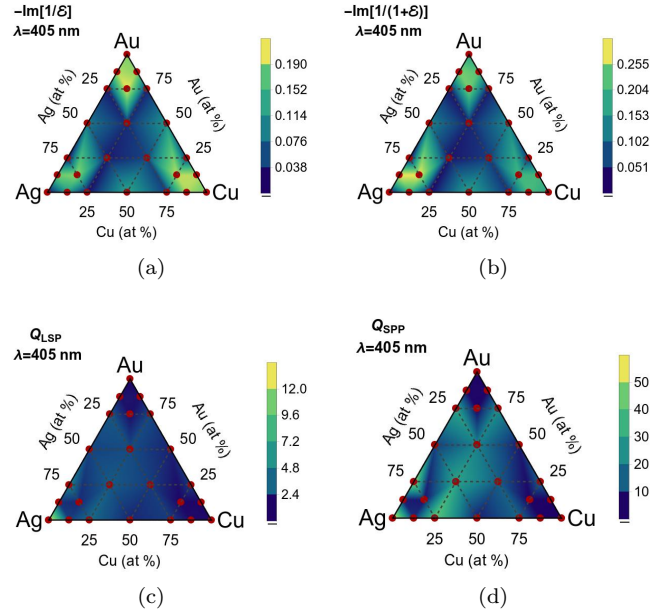


FIG. 13. Stoichiometric dependence of the averaged plasmon descriptors of bulk and surface EELS, Q_{LSP} , and Q_{SPP} for $\text{Au}_x\text{Ag}_y\text{Cu}_{1-x-y}$ at the common blu-ray solid-state laser wavelength 405 nm.

The second frequency is that of the common lasers used in blu-ray devices at 405 nm (3.0613 eV), generally produced using InGaN¹⁰² for efficient optical recording in conjunction with noble metal nano-clusters¹⁰³. In Fig. 13, {7:1:0} stoichiometric ratios show relatively significant plasmon resonance alongside {6:1:1} stoichiometric ratios in order of $\sim 10^{-1}$, which are comparable to these of maximums of plasmon peaks of binary alloys, with large quality factors of LSP and SPP. Ag predominantly has long-lived LSP, while AuAg_3 shows some longevity.

Lastly, the deep-UV laser at 290 nm (4.2753 eV) commonly produced in Ce:LiSAF / Ce:LiCAF media with Nd:YAG lasers¹⁰⁴ was presented for the sake of discussion. In Fig. 14, the bulk and surface EELS profiles here have structures but still a stronger response in Ag, Au, Au_6AgCu , and AuAg_6Cu , with a newly arising strong response in AuAg as shown. Correspondingly, AuAg has

short-lived LSP and SPP as does Ag, which performs relatively better in the former case as at the blu-ray laser.

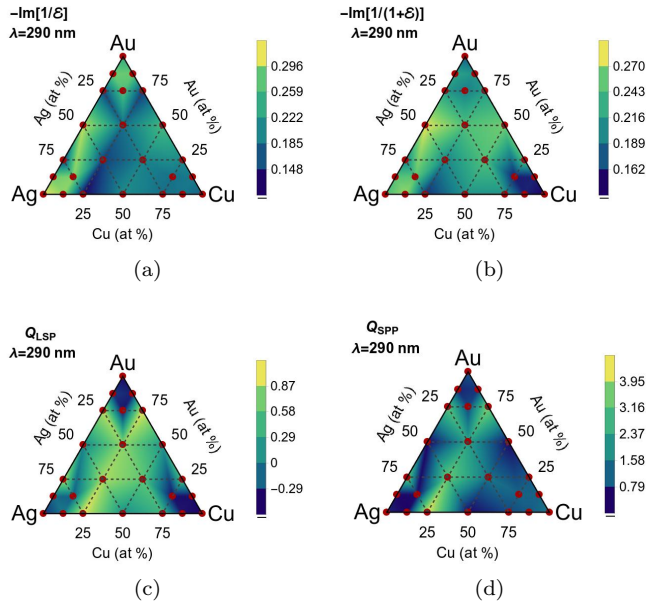


FIG. 14. Stoichiometric dependence of the averaged plasmon descriptors of bulk and surface EELS, Q_{LSP} , and Q_{SPP} for $Au_xAg_yCu_{1-x-y}$ at the common deep-UV solid-state laser wavelength 290nm.

The plasmonic responses of $Au_xAg_yCu_{1-x-y}$ have complex behaviours, which cannot be simply interpolated based on the stoichiometric ratios alone, despite the similar electronic structures of constituting atoms. Consistent first-principles simulations are thus essential to engineer and predict comprehensive alloy systems with well-controlled approximations at reasonable computational costs.

VII. CONCLUSION

It was shown that RPA starting from the KS band-structure fails to acceptably locate peaks in the absorption spectra of Au, Ag, and Cu, whereas RPA starting even from an approximate QP band-structure performs drastically better by locating low-energy peaks accurately in absorption spectra. Such an approximate QP band-structure can be achieved with little additional computational costs by applying some average stretching to bands via stretching operators, which can be obtained within G_0W_0 for a small set of grid points in the Brillouin zone and bands around the Fermi level. Despite their lack of finite size and surface effects, the bulk dielectric functions were used to determine some preliminary optic merits for LSP and SPP at plasmon resonance wavelengths. At the common solid-state red laser around 650 nm, $AuAgCu_6$, Au_6AgCu , $AuCu_7$, and Au_7Cu show relatively strong plasmon resonances,

whereas higher Ag concentrations reduce plasmon resonance in general. $AuAg_6Cu$ and $AuAu_7$ as well as $AuAg$, $AuCu$, and $AgCu$ alloys start showing stronger plasmon resonances with significant quality factors for LSP and SPP at the common blu-ray laser at 405 nm. This trend at 405 nm becomes more distinctive at deep-UV laser wavelengths around 290 nm. Particularly, pure Ag, $AuAg_7$, Ag_7Cu produce significant plasmon resonances with high LSP and SPP quality factors at 290 nm. Combining RPA starting an approximate QP band-structure with the Drude-Lorentz model using the semi-classical Drude parameters provide a computationally feasible approach to investigate spectra and plasmonic responses of the noble metals and their alloys. Despite its simplicity, some preliminary optic merits can be obtained that are useful as a starting point for tailoring plasmonic responses in such systems.

We gratefully acknowledge the support of Trinity College Dublin’s Studentship Award and School of Physics. We acknowledge and thank Tonatiuh Rangel and Daniele Varsano for discussions. We also acknowledge the DJEI/DES/SFI/HEA Irish Centre for High-End Computing (ICHEC) for the provision of computational facilities and support. We finally acknowledge the Trinity Centre for High Performance Computing and Science Foundation Ireland for the maintenance and funding, respectively, of the Boyle cluster on which further calculations were performed.

REFERENCES

- ¹C. Black, S. Gates, C. Murray, and S. Sun, “Magnetic storage medium formed of nanoparticles,” (2000).
- ²K.-S. Lee and M. A. El-Sayed, “Gold and silver nanoparticles in sensing and imaging: sensitivity of plasmon response to size, shape, and metal composition,” *The Journal of Physical Chemistry B* **110**, 19220–19225 (2006).
- ³P. K. Jain, X. Huang, I. H. El-Sayed, and M. A. El-Sayed, “Noble metals on the nanoscale: Optical and photothermal properties and some applications in imaging, sensing, biology, and medicine,” *Accounts of Chemical Research* **41**, 1578–1586 (2008).
- ⁴J. Zou, K. Gao, W. Challener, M. Ostrowski, V. Inturi, T. Zhao, and M. Kautzky, “Recording head for heat assisted magnetic recording with diffusion barrier surrounding a near field transducer,” (2014).
- ⁵S. Medici, M. Peana, V. M. Nurchi, J. I. Lachowicz, G. Crisponi, and M. A. Zoroddu, “Noble metals in medicine: Latest advances,” *Coordination Chemistry Reviews* **284**, 329 – 350 (2015).
- ⁶I. Sato, T. Oike, and N. Hanashima, “Heat assisted magnetic recording head and heat assisted magnetic recording apparatus for heating a recording region in a magnetic recording medium during magnetic recording,” (2009), uS Patent 7,538,978.
- ⁷X. Liu, A. Wang, X. Wang, C.-Y. Mou, and T. Zhang,

- “Au-cu alloy nanoparticles confined in sba-15 as a highly efficient catalyst for co oxidation,” *Chemical communications*, 3187–3189 (2008).
- ⁸M. Valodkar, S. Modi, A. Pal, and S. Thakore, “Synthesis and anti-bacterial activity of cu, ag and cuag alloy nanoparticles: A green approach,” *Materials Research Bulletin* **46**, 384 – 389 (2011).
 - ⁹B. Dastmalchi, P. Tassin, T. Koschny, and C. M. Soukoulis, “A new perspective on plasmonics: Confinement and propagation length of surface plasmons for different materials and geometries,” *Advanced Optical Materials* **4**, 177–184 (2016).
 - ¹⁰P. R. Wessel, “Reflectivity of silver-gold alloys in the spectral region 1.8–5.0 eV,” *Phys. Rev.* **132**, 2062–2064 (1963).
 - ¹¹A. J. McAlister, E. A. Stern, and J. C. McGroddy, “Faraday effect and fermi surfaces of the silver-gold alloy system,” *Phys. Rev.* **140**, A2105–A2109 (1965).
 - ¹²R. Stahl, H.-J. Spranger, and H.-P. Aubauer, “Optical properties of ordered auct₃,” *Z METALLKUNDE* **60**, 933–938 (1969).
 - ¹³H. Fukutani, “Optical constants of silver-gold alloys,” *Journal of the Physical Society of Japan* **30**, 399–403 (1971).
 - ¹⁴D. Beaglehole and E. Erlbach, “Electronic structure of noble-metal-noble-metal alloys,” *Phys. Rev. B* **6**, 1209–1225 (1972).
 - ¹⁵J. Rivory, “Optical properties of metastable agcu alloy films,” *Thin Solid Films* **37**, 345 – 350 (1976).
 - ¹⁶Y. Nishijima and S. Akiyama, “Unusual optical properties of the au/ag alloy at the matching mole fraction,” *Opt. Mater. Express* **2**, 1226–1235 (2012).
 - ¹⁷Y. Nishijima, Y. Hashimoto, G. Seniutinas, L. Rosa, and S. Juodkazis, “Engineering gold alloys for plasmonics,” *Applied Physics A* **117**, 641–645 (2014).
 - ¹⁸C. Gong and M. S. Leite, “Noble metal alloys for plasmonics,” *ACS Photonics* **3**, 507–513 (2016).
 - ¹⁹Y. Hashimoto, G. Seniutinas, A. Balčytis, S. Juodkazis, and Y. Nishijima, “Au-ag-cu nano-alloys: tailoring of permittivity,” *Scientific reports* **6** (2016).
 - ²⁰O. P. na Rodríguez, M. Caro, A. Rivera, J. Olivares, J. M. Perlado, and A. Caro, “Optical properties of au-ag alloys: An ellipsometric study,” *Opt. Mater. Express* **4**, 403–410 (2014).
 - ²¹S. L. Adler, “Quantum theory of the dielectric constant in real solids,” *Phys. Rev.* **126**, 413–420 (1962).
 - ²²N. Wiser, “Dielectric constant with local field effects included,” *Phys. Rev.* **129**, 62–69 (1963).
 - ²³P. A. Dirac, “The quantum theory of the emission and absorption of radiation,” in *Proceedings of the Royal Society of London A: Mathematical, Physical and Engineering Sciences*, Vol. 114 (The Royal Society, 1927) pp. 243–265.
 - ²⁴D. Bohm and D. Pines, “A collective description of electron interactions. i. magnetic interactions,” *Phys. Rev.* **82**, 625–634 (1951).
 - ²⁵D. Pines and D. Bohm, “A collective description of electron interactions: Ii. collective vs individual particle aspects of the interactions,” *Phys. Rev.* **85**, 338–353 (1952).
 - ²⁶D. Bohm and D. Pines, “A collective description of electron interactions: Iii. coulomb interactions in a degenerate electron gas,” *Phys. Rev.* **92**, 609–625 (1953).
 - ²⁷A. D. McLACHLAN and M. A. BALL, “Time-dependent hartree-fock theory for molecules,” *Rev. Mod. Phys.* **36**, 844–855 (1964).
 - ²⁸A. Marini, *Optical and electronic properties of Copper and Silver: from Density Functional Theory to Many Body Effects*, Ph.D. thesis, PhD Dissertation, University of Rome-Tor Vergata (2001).
 - ²⁹P. Drude, “Zur elektronentheorie der metalle,” *Annalen der Physik* **306**, 566–613 (1900).
 - ³⁰P. Drude, “Zur elektronentheorie der metalle; ii. teil. galvanomagnetische und thermomagnetische effecte,” *Annalen der Physik* **308**, 369–402 (1900).
 - ³¹H. A. Lorentz, *The Theory of Electrons and Its Applications to the Phenomena of Light and Radiant Heat: A Course of Lectures Delivered in Columbia University, New York, in March and April, 1906*, Vol. 29 (Columbia University Press, 1909).
 - ³²M. Fox, *Optical properties of solids*, Vol. 3 (Oxford university press, 2010).
 - ³³M. A. Ordal, R. J. Bell, R. W. Alexander, L. L. Long, and M. R. Querry, “Optical properties of fourteen metals in the infrared and far infrared: Al, co, cu, au, fe, pb, mo, ni, pd, pt, ag, ti, v, and w,” *Appl. Opt.* **24**, 4493–4499 (1985).
 - ³⁴E. J. Zeman and G. C. Schatz, “An accurate electromagnetic theory study of surface enhancement factors for silver, gold, copper, lithium, sodium, aluminum, gallium, indium, zinc, and cadmium,” *The Journal of Physical Chemistry* **91**, 634–643 (1987).
 - ³⁵I. R. Hooper and J. R. Sambles, “Dispersion of surface plasmon polaritons on short-pitch metal gratings,” *Phys. Rev. B* **65**, 165432 (2002).
 - ³⁶S. Berciaud, L. Cognet, P. Tamarat, and B. Lounis, “Observation of intrinsic size effects in the optical response of individual gold nanoparticles,” *Nano Letters* **5**, 515–518 (2005).
 - ³⁷N. Grady, N. Halas, and P. Nordlander, “Influence of dielectric function properties on the optical response of plasmon resonant metallic nanoparticles,” *Chemical Physics Letters* **399**, 167 – 171 (2004).
 - ³⁸M. Kreiter, S. Mittler, W. Knoll, and J. R. Sambles, “Surface plasmon-related resonances on deep and asymmetric gold gratings,” *Phys. Rev. B* **65**, 125415 (2002).
 - ³⁹M. G. Blaber, M. D. Arnold, and M. J. Ford, “Search for the ideal plasmonic nanoshell: The effects of surface scattering and alternatives to gold and silver,” *The Journal of Physical Chemistry C* **113**, 3041–3045 (2009).
 - ⁴⁰R. T. Beach and R. W. Christy, “Electron-electron scattering in the intraband optical conductivity of cu, ag, and au,” *Phys. Rev. B* **16**, 5277–5284 (1977).
 - ⁴¹M. H. Cohen, “Optical constants, heat capacity and

- the fermi surface,” *Philosophical Magazine* **3**, 762–775 (1958).
- ⁴²P. Hohenberg and W. Kohn, “Inhomogeneous electron gas,” *Phys. Rev.* **136**, B864–B871 (1964).
 - ⁴³W. Kohn and L. J. Sham, “Self-consistent equations including exchange and correlation effects,” *Phys. Rev.* **140**, A1133–A1138 (1965).
 - ⁴⁴D. C. Langreth and J. P. Perdew, “Theory of nonuniform electronic systems. i. analysis of the gradient approximation and a generalization that works,” *Phys. Rev. B* **21**, 5469–5493 (1980).
 - ⁴⁵J. P. Perdew, “Density-functional approximation for the correlation energy of the inhomogeneous electron gas,” *Phys. Rev. B* **33**, 8822–8824 (1986).
 - ⁴⁶J. P. Perdew, J. A. Chevary, S. H. Vosko, K. A. Jackson, M. R. Pederson, D. J. Singh, and C. Fiolhais, “Atoms, molecules, solids, and surfaces: Applications of the generalized gradient approximation for exchange and correlation,” *Phys. Rev. B* **46**, 6671–6687 (1992).
 - ⁴⁷L. Landau, “The theory of a fermi liquid,” *Soviet Physics JETP-USSR* **3**, 920–925 (1957).
 - ⁴⁸L. Landau, “Oscillations in a fermi liquid,” *SOVIET PHYSICS JETP-USSR* **5**, 101–108 (1957).
 - ⁴⁹L. Landau, “On the theory of the fermi liquid,” *Sov. Phys. JETP* **8**, 70 (1959).
 - ⁵⁰M. Rohlfing and S. G. Louie, “Electron-hole excitations in semiconductors and insulators,” *Phys. Rev. Lett.* **81**, 2312–2315 (1998).
 - ⁵¹A. Marini, R. Del Sole, and A. Rubio, “Bound excitons in time-dependent density-functional theory: Optical and energy-loss spectra,” *Phys. Rev. Lett.* **91**, 256402 (2003).
 - ⁵²F. Sottile, *Response functions of semiconductors and insulators: from the Bethe-Salpeter equation to time-dependent density functional theory*, Ph.D. thesis, Ecole Polytechnique X (2003).
 - ⁵³L. Reining, V. Olevano, A. Rubio, and G. Onida, “Excitonic effects in solids described by time-dependent density-functional theory,” *Phys. Rev. Lett.* **88**, 066404 (2002).
 - ⁵⁴S. Botti, F. Sottile, N. Vast, V. Olevano, L. Reining, H.-C. Weissker, A. Rubio, G. Onida, R. Del Sole, and R. W. Godby, “Long-range contribution to the exchange-correlation kernel of time-dependent density functional theory,” *Phys. Rev. B* **69**, 155112 (2004).
 - ⁵⁵S. Massidda, A. Continenza, M. Posternak, and A. Baldereschi, “Band-structure picture for mmo reexplored: A model *GW* calculation,” *Phys. Rev. Lett.* **74**, 2323–2326 (1995).
 - ⁵⁶S. Massidda, A. Continenza, M. Posternak, and A. Baldereschi, “Quasiparticle energy bands of transition-metal oxides within a model *gw* scheme,” *Phys. Rev. B* **55**, 13494–13502 (1997).
 - ⁵⁷A. Continenza, S. Massidda, and M. Posternak, “Self-energy corrections in VO_2 within a model *GW* scheme,” *Phys. Rev. B* **60**, 15699–15704 (1999).
 - ⁵⁸R. Godby, “Unoccupied electronic states,” *Topics in Applied Physics* **69** (1992).
 - ⁵⁹F. Aryasetiawan and O. Gunnarsson, “The *gw* method,” *Reports on Progress in Physics* **61**, 237 (1998).
 - ⁶⁰T. Rangel, D. Kecik, P. E. Trevisanutto, G.-M. Rignanese, H. Van Swygenhoven, and V. Olevano, “Band structure of gold from many-body perturbation theory,” *Phys. Rev. B* **86**, 125125 (2012).
 - ⁶¹H. Eckardt, L. Fritsche, and J. Noffke, “Self-consistent relativistic band structure of the noble metals,” *Journal of Physics F: Metal Physics* **14**, 97 (1984).
 - ⁶²A. J. Cohen, P. Mori-Sánchez, and W. Yang, “Challenges for density functional theory,” *Chemical Reviews* **112**, 289–320 (2012).
 - ⁶³A. Marini, G. Onida, and R. Del Sole, “Quasiparticle electronic structure of copper in the *GW* approximation,” *Phys. Rev. Lett.* **88**, 016403 (2001).
 - ⁶⁴A. Marini, R. Del Sole, and G. Onida, “First-principles calculation of the plasmon resonance and of the reflectance spectrum of silver in the *GW* approximation,” *Phys. Rev. B* **66**, 115101 (2002).
 - ⁶⁵A. Marini, R. Del Sole, A. Rubio, and G. Onida, “Quasiparticle band-structure effects on the d hole lifetimes of copper within the *gw* approximation,” *Phys. Rev. B* **66**, 161104 (2002).
 - ⁶⁶D. Pines, *Elementary excitations in solids* (Perseus, 1966).
 - ⁶⁷W. G. Aulbur, L. Jönsson, and J. W. Wilkins, “Quasiparticle calculations in solids,” *Solid State Physics* **54**, 1–218 (2000).
 - ⁶⁸A. L. Fetter and J. D. Walecka, *Quantum theory of many-particle systems* (Courier Corporation, 2012).
 - ⁶⁹E. L. Shirley and R. M. Martin, “*Gw*,” *Phys. Rev. B* **47**, 15404–15412 (1993).
 - ⁷⁰M. S. Hybertsen and S. G. Louie, “Electron correlation in semiconductors and insulators: Band gaps and quasiparticle energies,” *Phys. Rev. B* **34**, 5390–5413 (1986).
 - ⁷¹R. W. Godby and R. J. Needs, “Metal-insulator transition in kohn-sham theory and quasiparticle theory,” *Phys. Rev. Lett.* **62**, 1169–1172 (1989).
 - ⁷²P. Giannozzi, S. Baroni, N. Bonini, M. Calandra, R. Car, C. Cavazzoni, D. Ceresoli, G. L. Chiarotti, M. Cococcioni, I. Dabo, A. D. Corso, S. de Gironcoli, S. Fabris, G. Fratesi, R. Gebauer, U. Gerstmann, C. Gougoussis, A. Kokalj, M. Lazzeri, L. Martin-Samos, N. Marzari, F. Mauri, R. Mazurek, S. Paolini, A. Pasquarello, L. Paulatto, C. Sbraccia, S. Scandolo, G. Scialuzero, A. P. Seitsonen, A. Smogunov, P. Umari, and R. M. Wentzcovitch, “Quantum espresso: a modular and open-source software project for quantum simulations of materials,” *Journal of Physics: Condensed Matter* **21**, 395502 (2009).
 - ⁷³P. Giannozzi, O. Andreussi, T. Brumme, O. Bunau, M. B. Nardelli, M. Calandra, R. Car, C. Cavazzoni, D. Ceresoli, M. Cococcioni, N. Colonna, I. Carnimeo, A. D. Corso, S. de Gironcoli, P. Delugas,

- R. A. D. Jr, A. Ferretti, A. Floris, G. Fratesi, G. Fugallo, R. Gebauer, U. Gerstmann, F. Giustino, T. Gorni, J. Jia, M. Kawamura, H.-Y. Ko, A. Kokalj, E. Kkbenli, M. Lazzeri, M. Marsili, N. Marzari, F. Mauri, N. L. Nguyen, H.-V. Nguyen, A. O. de la Roza, L. Paulatto, S. Ponc, D. Rocca, R. Sabatini, B. Santra, M. Schlipf, A. P. Seitsonen, A. Smogunov, I. Timrov, T. Thonhauser, P. Umari, N. Vast, X. Wu, and S. Baroni, "Advanced capabilities for materials modelling with q uantum espresso," *Journal of Physics: Condensed Matter* **29**, 465901 (2017).
- ⁷⁴"Opium:the optimized pseudopotential interface unification module," <http://opium.sourceforge.net/>, accessed: 2017-11-30.
- ⁷⁵I.-K. Suh, H. Ohta, and Y. Waseda, "High-temperature thermal expansion of six metallic elements measured by dilatation method and x-ray diffraction," *Journal of Materials Science* **23**, 757–760 (1988).
- ⁷⁶N. Marzari, D. Vanderbilt, A. De Vita, and M. C. Payne, "Thermal contraction and disordering of the al(110) surface," *Phys. Rev. Lett.* **82**, 3296–3299 (1999).
- ⁷⁷R. Gurzhi, "On the theory of the infrared absorptivity of metals," *Soviet Physics JETP* **6**, 506–512 (1958).
- ⁷⁸R. Gurzhi, "Mutual electron correlations in metal optics," *Sov. Phys. JETP* **8**, 673–675 (1959).
- ⁷⁹A. Marini, C. Hogan, M. Grning, and D. Varsano, "yambo: An ab initio tool for excited state calculations," *Computer Physics Communications* **180**, 1392 – 1403 (2009).
- ⁸⁰D. Gall, "Electron mean free path in elemental metals," *Journal of Applied Physics* **119**, 085101 (2016).
- ⁸¹S. Babar and J. H. Weaver, "Optical constants of cu, ag, and au revisited," *Appl. Opt.* **54**, 477–481 (2015).
- ⁸²H. Boersch, H. Miessner, and W. Raith, "Untersuchungen zur winkelabhängigkeit des 14,7 ev-energieverlustes von elektronen in aluminium," *Zeitschrift für Physik* **168**, 404–410 (1962).
- ⁸³H. Raether, "Electron energy loss spectroscopy," *Springer Tracts in Modern Physics* **38**, 85 (1965).
- ⁸⁴H. Froitzheim, "Electron energy loss spectroscopy," in *Electron Spectroscopy for Surface Analysis*, edited by H. Ibach (Springer Berlin Heidelberg, Berlin, Heidelberg, 1977) pp. 205–250.
- ⁸⁵R. A. Ferrell, "Angular dependence of the characteristic energy loss of electrons passing through metal foils," *Phys. Rev.* **101**, 554–563 (1956).
- ⁸⁶M. G. Blaber, M. D. Arnold, and M. J. Ford, "A review of the optical properties of alloys and intermetallics for plasmonics," *Journal of Physics: Condensed Matter* **22**, 143201 (2010).
- ⁸⁷S. Anantha Ramakrishna and J. B. Pendry, "Removal of absorption and increase in resolution in a near-field lens via optical gain," *Phys. Rev. B* **67**, 201101 (2003).
- ⁸⁸M. D. Arnold and M. G. Blaber, "Optical performance and metallic absorption in nanoplasmonic systems," *Opt. Express* **17**, 3835–3847 (2009).
- ⁸⁹U. Kreibig and M. Vollmer, "Theoretical considerations," in *Optical Properties of Metal Clusters* (Springer Berlin Heidelberg, Berlin, Heidelberg, 1995) pp. 13–201.
- ⁹⁰H. Raether, "Surface plasmons on smooth surfaces," in *Surface Plasmons on Smooth and Rough Surfaces and on Gratings* (Springer Berlin Heidelberg, Berlin, Heidelberg, 1988) pp. 4–39.
- ⁹¹M. Kuttge, E. J. R. Vesseur, J. Verhoeven, H. J. Lezec, H. A. Atwater, and A. Polman, "Loss mechanisms of surface plasmon polaritons on gold probed by cathodoluminescence imaging spectroscopy," *Applied Physics Letters* **93**, 113110 (2008), <https://doi.org/10.1063/1.2987458>.
- ⁹²M. Rocca, "Low-energy eels investigation of surface electronic excitations on metals," *Surface Science Reports* **22**, 1 – 71 (1995).
- ⁹³C. Snnichsen, T. Franzl, T. Wilk, G. von Plessen, and J. Feldmann, "Plasmon resonances in large noble-metal clusters," *New Journal of Physics* **4**, 93 (2002).
- ⁹⁴A. J. Haes, S. Zou, G. C. Schatz, and R. P. Van Duyne, "A nanoscale optical biosensor: the long range distance dependence of the localized surface plasmon resonance of noble metal nanoparticles," *The Journal of Physical Chemistry B* **108**, 109–116 (2004).
- ⁹⁵A. V. Zayats, I. I. Smolyaninov, and A. A. Maradudin, "Nano-optics of surface plasmon polaritons," *Physics Reports* **408**, 131 – 314 (2005).
- ⁹⁶A. V. Zayats and I. I. Smolyaninov, "Near-field photonics: surface plasmon polaritons and localized surface plasmons," *Journal of Optics A: Pure and Applied Optics* **5**, S16 (2003).
- ⁹⁷N. Engheta, "Circuits with light at nanoscales: Optical nanocircuits inspired by metamaterials," *Science* **317**, 1698–1702 (2007).
- ⁹⁸K. F. MacDonald, Z. L. Sámson, M. I. Stockman, and N. I. Zheludev, "Ultrafast active plasmonics," *Nature Photonics* **3**, 55 EP – (2008).
- ⁹⁹A. V. Krasavin and N. I. Zheludev, "Active plasmonics: Controlling signals in au/ga waveguide using nanoscale structural transformations," *Applied Physics Letters* **84**, 1416–1418 (2004).
- ¹⁰⁰W. Koechner, *Solid-state laser engineering*, Vol. 1 (Springer, 2013).
- ¹⁰¹B. Kstner, M. Gellner, M. Schtz, F. Schppler, A. Marx, P. Strbel, P. Adam, C. Schmuck, and S. Schlcker, "Sers labels for red laser excitation: Silica-encapsulated sams on tunable gold/silver nanoshells," *Angewandte Chemie International Edition* **48**, 1950–1953 (2009).
- ¹⁰²S. Nakamura, M. Senoh, S. ichi Nagahama, N. Iwasa, T. Yamada, T. Matsushita, H. Kiyoku, and Y. Sugimoto, "Ingan-based multi-quantum-well-structure laser diodes," *Japanese Journal of Applied Physics* **35**, L74 (1996).
- ¹⁰³A. Royon, K. Bourhis, M. Bellec, G. Papon, B. Bousquet, Y. Deshayes, T. Cardinal, and L. Canioni, "Silver clusters embedded in glass as a perennial high ca-

- capacity optical recording medium,” [Advanced Materials](#) **22**, 5282–5286 (2010).
- ¹⁰⁴C. D. Marshall, J. A. Speth, S. A. Payne, W. F. Krupke, G. J. Quarles, V. Castillo, and B. H. T. Chai, “Ultraviolet laser emission properties of Ce^{3+} -doped LiSrAlF_6 and LiCaAlF_6 ,” [J. Opt. Soc. Am. B](#) **11**, 2054–2065 (1994).

Supporting Information

Plasmonic performances of $\text{Au}_x\text{Ag}_y\text{Cu}_{1-x-y}$ alloys using many-body perturbation theory

Okan K. Orhan, and David D. O'Regan

January 4, 2019

Contents

1	Sample crystal structures for the studied stoichiometric ratios	2
2	Drude Parameters	2
3	Stretching operators	4

1 Sample crystal structures for the studied stoichiometric ratios

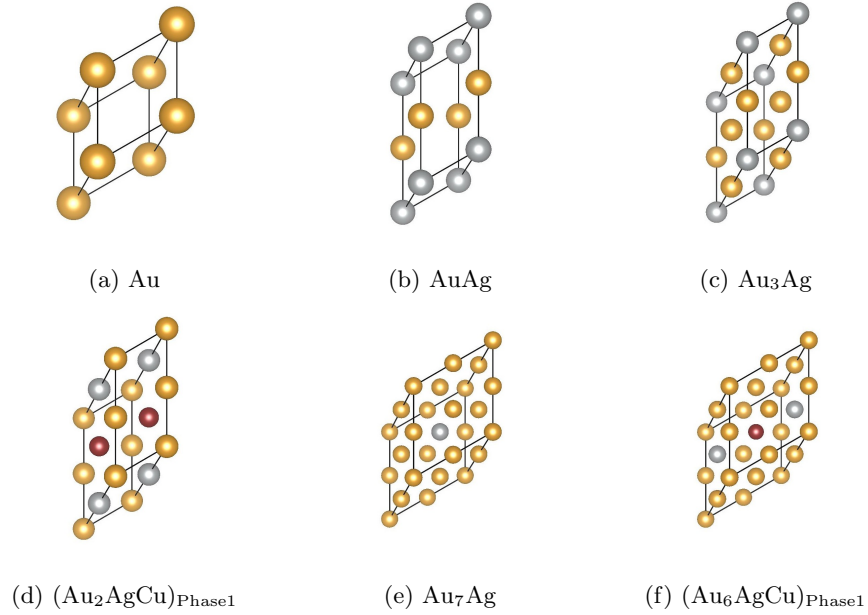


Figure 1: The sample structure for chosen stoichiometric ratios of $\text{Au}_x\text{Ag}_y\text{Cu}_{1-x-y}$.

2 Drude Parameters

	ω_p	η_p^{FGR}	$\varepsilon_\infty^{\text{FGR}}$	η_p^{RPA}	$\varepsilon_\infty^{\text{RPA}}$	$\omega_p^{\text{G}_0\text{W}_0}$	$\eta_p^{\text{G}_0\text{W}_0}$	$\varepsilon_\infty^{\text{G}_0\text{W}_0}$
Au	8.911	0.01990	2.143	0.01991	3.775	8.947	0.02266	1.601
Ag	8.725	0.01896	-4.436	0.01896	-2.610	8.925	0.01918	-2.624
Cu	8.836	0.02756	-2.988	0.02758	-0.688	9.313	0.02426	0.104

Table 1: The Drude parameters $\{\omega_p, \eta_p, \varepsilon_\infty\}$ (in eV, eV and dimensionless, respectively) for spectra using FGR, RPA, and $\text{G}_0\text{W}_0+\text{RPA}$ for pure Au, Ag, and Cu.

System	ω_p	η	ε_∞	System	ω_p	η	ε_∞
Au	8.947	0.02266	1.601	Au ₇ Ag	8.793	0.01992	1.073
Ag	8.925	0.01918	-2.624	Au ₇ Cu	8.708	0.01991	1.414
Cu	9.313	0.02426	0.1039	AuAg ₇	8.735	0.01748	-2.096
AuAg	10.36	0.02392	-0.5116	AuCu ₇	8.61	0.02041	0.291
AuCu	10.91	0.0252	0.8523	Ag ₇ Cu	8.918	0.01835	-2.283
AgCu	10.32	0.02466	-1.26	AgCu ₇	8.896	0.02108	-0.2371
Au ₃ Ag	12.8	0.0278	0.5446	Au ₆ AgCu (p1)	8.666	0.01969	0.8855
Au ₃ Cu	12.99	0.03062	1.227	Au ₆ AgCu (p2)	8.655	0.01963	0.8855
AuAg ₃	12.45	0.02519	-1.568	Au ₆ AgCu (p3)	8.634	0.01952	0.8855
AuCu ₃	12.41	0.02934	0.4781	Au ₆ AgCu (p4)	8.087	0.01788	0.8855
Ag ₃ Cu	12.58	0.02697	-1.942	AuAg ₆ Cu (p1)	8.571	0.01822	-1.755
AgCu ₃	12.51	0.02997	-0.5781	AuAg ₆ Cu (p2)	8.585	0.01828	-1.755
Au ₂ AgCu (p1)	12.64	0.02888	0.1703	AuAg ₆ Cu (p3)	8.614	0.01838	-1.755
Au ₂ AgCu (p2)	12.26	0.02872	0.1703	AuAg ₆ Cu (p4)	8.896	0.0184	-1.755
Au ₂ AgCu (p3)	12.26	0.02872	0.1703	AuAgCu ₆ (p1)	8.437	0.01975	-0.05001
AuAg ₂ Cu (p1)	11.97	0.02676	-0.8858	AuAgCu ₆ (p2)	8.445	0.01979	-0.05001
AuAg ₂ Cu (p2)	12.93	0.02774	-0.8858	AuAgCu ₆ (p3)	8.338	0.01949	-0.05001
AuAg ₂ Cu (p3)	12.92	0.02773	-0.8858	AuAgCu ₆ (p4)	8.246	0.01945	-0.05001
AuAgCu ₂ (p1)	12.84	0.02931	-0.2039				
AuAgCu ₂ (p2)	11.72	0.02738	-0.2039				
AuAgCu ₂ (p3)	11.73	0.02739	-0.2039				

Table 2: Drude parameters for Au_xAg_yCu_{1-x-y} .

3 Stretching operators

System	s_c	s_v	System	s_c	s_v
Au	0.825253	1.419797	Au ₇ Ag	0.967842	1.218996
Ag	0.846172	1.376302	Au ₇ Cu	0.959605	1.277749
Cu	0.809883	1.735804	AuAg ₇	0.972795	1.072632
AuAg	0.942895	1.245925	AuCu ₇	0.937301	1.459205
AuCu	0.921209	1.451945	Ag ₇ Cu	0.966574	1.138571
AgCu	0.921900	1.382942	AgCu ₇	0.932309	1.414183
Au ₃ Ag	0.945233	1.197529	Au ₆ AgCu (p1)	0.961430	1.272030
Au ₃ Cu	0.936102	1.329064	Au ₆ AgCu (p2)	0.961097	1.26530
AuAg ₃	0.951899	1.105431	Au ₆ AgCu (p3)	0.961277	1.266095
AuCu ₃	0.922466	1.454606	Au ₆ AgCu (p4)	0.959646	1.268756
Ag ₃ Cu	0.945817	1.215392	AuAg ₆ Cu (p1)	0.965500	1.168711
AgCu ₃	0.935669	1.382684	AuAg ₆ Cu (p2)	0.965551	1.177290
Au ₂ AgCu (p1)	0.936355	1.302908	AuAg ₆ Cu (p3)	0.974523	1.185852
Au ₂ AgCu (p2)	0.931013	1.311556	AuAg ₆ Cu (p4)	0.965523	1.174112
Au ₂ AgCu (p3)	0.930925	1.311619	AuAgCu ₆ (p1)	0.936233	1.404183
AuAg ₂ Cu (p1)	0.938311	1.272339	AuAgCu ₆ (p2)	0.943095	1.399728
AuAg ₂ Cu (p2)	0.934446	1.261742	AuAgCu ₆ (p3)	0.936821	1.403408
AuAg ₂ Cu (p3)	0.934076	1.261342	AuAgCu ₆ (p4)	0.943707	1.407826
AuAgCu ₂ (p1)	0.933284	1.382637			
AuAgCu ₂ (p2)	0.936700	1.371520			
AuAgCu ₂ (p3)	0.936793	1.372440			

Table 3: First-principles G_0W_0 stretching operators for conduction and valance bands of $\text{Au}_x\text{Ag}_y\text{Cu}_{1-x-y}$.